



Time-dependent Ionization in a Steady Flow in an MHD Model of the Solar Corona and Wind

Chengcai Shen¹, John C. Raymond¹ , Zoran Mikić², Jon A. Linker², Katharine K. Reeves¹ , and Nicholas A. Murphy¹ 

¹Harvard-Smithsonian Center for Astrophysics, 60 Garden Street, Cambridge, MA 02138, USA

²Predictive Science, Inc. (PSI), San Diego, CA 92121-2910, USA

Received 2016 February 12; revised 2017 October 12; accepted 2017 October 13; published 2017 November 14

Abstract

Time-dependent ionization is important for diagnostics of coronal streamers and pseudostreamers. We describe time-dependent ionization calculations for a three-dimensional magnetohydrodynamic (MHD) model of the solar corona and inner heliosphere. We analyze how non-equilibrium ionization (NEI) influences emission from a pseudostreamer during the Whole Sun Month interval (Carrington rotation CR1913, 1996 August 22 to September 18). We use a time-dependent code to calculate NEI states, based on the plasma temperature, density, velocity, and magnetic field in the MHD model, to obtain the synthetic emissivities and predict the intensities of the Ly α , O VI, Mg X, and Si XII emission lines observed by the *SOHO*/Ultraviolet Coronagraph Spectrometer (UVCS). At low coronal heights, the predicted intensity profiles of both Ly α and O VI lines match UVCS observations well, but the Mg X and Si XII emission are predicted to be too bright. At larger heights, the O VI and Mg X lines are predicted to be brighter for NEI than equilibrium ionization around this pseudostreamer, and Si XII is predicted to be fainter for NEI cases. The differences of predicted UVCS intensities between NEI and equilibrium ionization are around a factor of 2, but neither matches the observed intensity distributions along the full length of the UVCS slit. Variations in elemental abundances in closed field regions due to the gravitational settling and the FIP effect may significantly contribute to the predicted uncertainty. The assumption of Maxwellian electron distributions and errors in the magnetic field on the solar surface may also have notable effects on the mismatch between observations and model predictions.

Key words: atomic processes – Sun: corona – Sun: UV radiation

1. Introduction

There are two kinds of coronal streamers: helmet streamers and pseudostreamers. Helmet streamers separate coronal holes of opposite magnetic polarity, whereas pseudostreamers usually occur over twin loop arcades and separate coronal holes of the same polarity. From white-light observations—for instance, by the Large Angle and Spectrometric Coronagraph (LASCO; Brueckner et al. 1995)—pseudostreamers extend high into the corona and appear similar to helmet streamers in white light. The multiple sheets inside pseudostreamers contribute to the K coronal brightness. The flow around pseudostreamers seems to be relatively stable in that they persist for weeks, and the highest outflow speed can reach a few hundred kilometers per second (Abbo et al. 2015). Rachmeler et al. (2014) observed a hybrid structure that contained both a streamer and a pseudostreamer, highlighting the complexity of magnetic structures in the corona.

Pseudostreamers have somewhat different properties than streamers, though only a modest number of them have been analyzed. Abbo et al. (2015) used data from the Ultraviolet Coronagraph Spectrometer (UVCS) on the *SOHO* satellite (Kohl et al. 1997) to show that the O VI kinetic temperature was higher and the density lower than in bipolar streamers, placing them in between fast and slow wind regimes. Therefore, Abbo et al. described it as a hybrid type of flow. Wang et al. (2012) found a range of speeds from 350 to 550 km s⁻¹ and temperatures derived from the O⁷⁺/O⁶⁺ ratio at 1 au intermediate between fast and slow wind values. Zhao et al. (2013) found regions of very high proton density and strong radial magnetic field associated with pseudostreamers in *Ulysses* data. The temperature derived from the O⁷⁺/O⁶⁺ ratio

follows the same anti-correlation with wind speed as does the rest of the solar wind, but it is somewhat displaced toward lower speeds and higher temperatures.

In some coronal environments, the plasma does not have sufficient time to reach ionization equilibrium, either due to rapid changes in temperature (as in nanoflares and CMEs), or due to fast motion of the plasma through gradients in density and temperature in the corona. Normally, the changes of the population fraction of a particular ion are the consequence of both ionization and recombination, and the ionization and recombination rate coefficients depend strongly on the electron temperature. More precisely, they depend on the electron thermal energy distribution. In the case where plasma temperature remains constant for a long time or changes slowly, the plasma will reach ionization equilibrium. However, in the cases where rapid changes (in the Lagrangian sense) in plasma temperature occur, the dynamical timescale of the plasma can be significantly shorter than the ionization or recombination timescales. As a result, the ionization and recombination processes do not have sufficient time to drive the ionic populations to their equilibrium state. The plasma is then in a non-equilibrium ionization (NEI) state, and the ionization fractions must be obtained by solving time-dependent ionization equations. NEI will cause errors in the analysis of spectroscopic observations if equilibrium is assumed, but it can also be used as a diagnostic in its own right because the ionization state contains information about the thermal history of the plasma (Murphy et al. 2011).

Two ideas have been proposed to explain the formation mechanism of solar wind in pseudostreamers and bipolar streamers. One is expansion factor models in which the properties of the solar wind vary because of different flow

geometry or variation in the deposition of energy and momentum along open field lines. Wang et al. (2012) focus on the role of the expansion factor of magnetic flux tubes in determining solar wind speed and density; they point out that pseudostreamers have lower cusps, leading to more rapid expansion at low heights and re-collimation at larger heights. Riley & Luhmann (2012) compare predictions based on the low overall expansion factors of pseudostreamers and predictions based on distance from the coronal hole boundary with in situ measurements of density and velocity in a unipolar streamer. Another set of ideas centers on interchange reconnection to inject FIP-enhanced plasma from closed magnetic loops into the solar wind, providing an explanation for the FIP abundance anomaly (Schwadron et al. 1999). This idea has been related to the S-web of small-scale magnetic reversals (Antiochos et al. 2011; Linker et al. 2011). In addition, Stakhiv et al. (2015) reported a quasi-stationary solar wind state that has charge state characteristics similar to slow wind, but with an elemental composition that is coronal hole-like. If the plasma resides in closed loops long enough, it tends to approach ionization equilibrium, leading to very different ionization states than in the steady-flow case, though other considerations such as suprathermal electrons could also affect the ionization state (Ko et al. 1998; Esser & Edgar 2001; Oran et al. 2015). In either case, the oxygen ionization state of the solar wind is frozen-in at about $2 R_{\odot}$, so that the O^{7+}/O^{6+} ratio is sensitive to the electron temperature and density, as well as the oxygen velocity, through the freeze-in region; the degree of departure from ionization equilibrium provides information about the plasma parameters there.

The ionization states in pseudostreamers and the solar wind have been reported in several studies. In early models, charge state calculations from a coronal model were reported by Cranmer et al. (2007). They later made important steps in predicting charge states in an MHD model due to supra-thermal electrons (Cranmer 2014). Jin et al. (2012) made a charge state calculation in a global MHD model and compared several ionic charge states observed in situ with the *ACE* to the model prediction. Abbo et al. (2015) studied a pseudostreamer and a helmet streamer during Carrington rotation 2067 by analyzing spectroscopic UVCS observations from 2008 March 12–17. The solar wind plasma parameters, including kinetic temperature, were determined by analyzing O VI doublet and Ly α observations, and electron density and outflow velocity were derived from an MHD model. They compared the physical parameters of pseudostreamers and bipolar streamers, and found higher kinetic temperature, higher outflow velocities of O VI ions, and lower electron density values for pseudostreamers under the assumption of ionization equilibrium.

Time-dependent ionization also has been investigated for the analysis of both remote sensing observations and in situ measurements. Landi et al. (2014) and Oran et al. (2015) computed the ionization states with the AWSoM model (Oran et al. 2013; Sokolov et al. 2013; van der Holst et al. 2014; Meng et al. 2015) and compared them with SUMER (Wilhelm et al. 1995) or EIS (Culhane et al. 2007) observations at low heights and in situ *Ulysses*/SWICS (Gloeckler et al. 1992) charge state measurements at large distances. Oran et al. (2015) made post-processing time-dependent ionization calculations and compared the simulation to spectra very close to the solar surface from EIS and with *Ulysses* measurements of the C^{6+}/C^{5+} and O^{7+}/O^{6+} ratios. They found that the discrepancy

of ionization states between predictions and observations can be decreased by considering non-Maxwellian electron distributions (Laming & Lepri 2007; Cranmer 2014). They also considered other possible explanations: electron densities higher than in the model or lower speeds along the magnetic field lines, either as a result of slower bulk acceleration or ion speeds lower than the proton speed. Oran et al. (2015) also discussed the ionization states in a pseudostreamer and showed that the pseudostreamer produces a higher O^{7+}/O^{6+} ratio (around 0.2) than along other open field lines. Although it is not easy to directly estimate the effects of time-dependent ionization using observational data, time-dependent ionization is an essential physical process and has important impacts on both remote sensing observations and in situ measurements.

In a previous study (Shen et al. 2013), we calculated the time-dependent ionization state for an MHD simulation of magnetic reconnection in a CME (Reeves et al. 2010), and we predicted the EUV emission line intensities and the count rates in *SDO*/AIA bands. At low heights, the predicted intensities of the AIA 94 and 131 Å channels are fainter for NEI than for equilibrium ionization, but the reverse is true for the cooler AIA channels. At large heights, AIA 94 and 131 Å intensities are higher for NEI than for equilibrium ionization in the current sheet, and again the reverse is true for the cooler AIA channels. Temperatures from AIA are typically derived from differential emission measures that employ all six AIA EUV bandpasses (e.g., Hanneman & Reeves 2014; Reeves et al. 2017). Because the AIA 94 and 131 Å channels are the only two AIA channels that detect hot plasma well, using the assumption of ionization equilibrium to derive electron temperatures would lead to a significant underestimate of the temperature low in the current sheet and an overestimate at larger heights.

In this paper, we concentrate on UVCS observations in the inner corona (e.g., $1.41 R_{\odot} \sim 3.93 R_{\odot}$) where the ionization state of the plasma evolves from equilibrium toward frozen-in (Hundhausen et al. 1968) at the densities and velocities in streamers. We address several questions. At what height does NEI begin to significantly affect predicted line intensities? Which lines are weakly or strongly affected? How large an effect does emission from surrounding structures along the LOS have on the line intensities—and therefore on derived coronal parameters? In general, we do not have enough observational constraints to use NEI as an independent diagnostic, but NEI calculations are essential to making self-consistent model predictions. In Section 2, we describe the coronal MHD model and NEI calculations. In Section 3, we present our results, and we present our conclusions in Section 4.

2. Method

2.1. Description of the Coronal MHD Model

In this work, we apply the time-dependent ionization analysis to a 3D MHD simulation and investigate the properties of NEI in a coronal pseudostreamer. For our analysis, we chose the Whole Sun Month (WSM) interval, which occurred during Carrington rotation (CR) 1913 (from 1996 August 22–September 18) because it contained a pseudostreamer that was observed with the LASCO C2 and UVCS instruments on *SOHO*. An earlier version of our MHD model, employing a polytropic energy equation (Mikić et al. 1999), was used to analyze WSM, and in particular to compare the simulated

white-light polarization brightness to MLSO MK3 images (Linker et al. 1999). The simulated structures, including the position and shape of the streamer belt, coronal hole boundaries, and the heliospheric current sheet, were in reasonable agreement with observations from the *SOHO*, *Ulysses*, and *WIND* spacecraft, though some differences were present. The polytropic model was also used by Abbo et al. (2015) to study a pseudostreamer and a helmet streamer during CR2067.

In this work, we use an improved version of the MHD model that has a more accurate description of energy flow in the corona. This newer MAS model uses an improved energy equation that contains parameterized coronal heating, parallel thermal conduction, radiative losses, and the acceleration of the solar wind by Alfvén waves (Lionello et al. 2009). The model uses observations of the photospheric magnetic field as the lower boundary condition. We used a synoptic photospheric magnetic field map for CR1913 from the MDI instrument on *SOHO*. Lionello et al. (2009) used this model with an improved energy equation to investigate different heating models, also for the WSM time frame. With this improved model, it became possible to make quantitative comparisons with emission in EUV from the EIT instrument on *SOHO*, and with X-ray emission from the soft X-ray telescope on Yohkoh. These comparisons were used to evaluate three different coronal heating models.

In the work of Lionello et al. (2009), the EUV intensities were calculated based on an assumption of equilibrium ionization. In general, time-dependent ionization (i.e., NEI) can lead to significant differences in predicted emission in coronal regions, especially in regions where the flow speed is high, or where the coronal plasma is changing state rapidly, such as in outflow regions associated with magnetic reconnection. This was investigated in a simplified 2D axisymmetric eruption (Shen et al. 2013). In this paper, we study the effect of NEI on a more realistic 3D structure. The MHD model in this work used a larger number of mesh points than the Lionello et al. (2009) model, with a mesh of $221 \times 275 \times 431$ points, and correspondingly included more small-scale structures in the photospheric magnetic field. The smallest radial-grid interval at the solar surface was 20 km. We have developed two principal heating models (Versions 1 and 2). Version 1 of the model is described by Lionello et al. (2009). In the present paper, we have used Version 2 of the heating model, which was used in our prediction of the state of the corona prior to the 2010 July 11 total solar eclipse.³ The heating is the sum of four terms. The first is an active-region and quiet-Sun term in which the heating falls off exponentially from the solar surface with a scale height of $\lambda = 0.06 R_{\odot}$, with an amplitude that is proportional to B_{photo} , the local magnitude of the photospheric magnetic field. This heating is used only in closed-field regions, as estimated from a PFSS model. The second term is a “neutral line” heating whose magnitude falls away from the photospheric polarity inversion line ($B_r = 0$). This heating has a scale length $\lambda = 0.03 R_{\odot}$, and is also proportional to B_{photo} . The third term is a “fast wind” heating with a scale length $\lambda = 1.0 R_{\odot}$ that is applied everywhere. The fourth term is a “short-scale” heating with a scale length $\lambda = 0.03 R_{\odot}$ that is also applied everywhere. It should be kept in mind that this is still a single-fluid model, and that the assumption of equal

electron and ion temperatures may introduce significant errors. Henceforth, we assume that the electron temperature (and ion temperature) is equal to the (single) temperature in the model.

We integrate the MHD equations until the large-scale magnetic topology ceases to change substantially, and the magnetic and kinetic energies approach asymptotic values. At the end of the run, these energies are steady to within $\sim 1\%$ or so. It is important to note that a true steady state may not exist. We have found that the loops in active regions can experience repeating cycles of thermal nonequilibrium in which the plasma experiences repeated periodic cycles (e.g., as described by Mikić et al. 2013). This has been seen in our global simulations as well, and occurs in the simulation we used in the present work. However, this non-steady behavior does not substantially affect the charge states along the open field lines on which we concentrate in this paper.

Other global coronal and solar wind models have also included sophisticated treatments of energy transport, multi-fluid descriptions of the plasma, and different heating prescriptions. For example, a four-fluid three-dimensional MHD global heliospheric model developed by Usmanov et al. (2016) includes turbulence transport equations based on Reynolds decomposition, coupled with the mean-flow Reynolds-averaged equations. Sokolov et al. (2013), Oran et al. (2013), van der Holst et al. (2014), and Meng et al. (2015) describe the AWSoM model, in which the coronal heating and solar wind acceleration are modeled via low-frequency Alfvén wave turbulence. Because our focus is not to compare different models, but to investigate the extent to which time-dependent ionization is required to predict emission spectra and charge states, we will not discuss the merits of different treatments of the microphysics.

2.2. NEI Calculation

Once the MHD simulations have been completed, we use the results to perform time-dependent ionization calculations by solving equations for the evolution of the ionization fractions of the ions of interest. The MHD simulation determines the steady-state solution by relaxing the structure in time until the corona reaches a steady state. The temperature, density, and plasma velocity are then known. Under the assumption that the plasma is optically thin, the properties of emission lines along the line of sight (LOS) can be predicted from the local electron density, temperature, and ionization states. To get ion charge states from this simulation, we need to solve the time-dependent ionization equations.

The charge state evolution of the atom with atomic number Z is given by the following equations:

$$\frac{df_i}{dt} = n_e [C(T_e)_{i-1} f_{i-1} - (C(T_e)_i + R(T_e)_i) f_i + R(T_e)_i f_{i+1}] \quad (1)$$

where f_i is the ionic fraction of a given atomic species in the i th ionization state (where $i = 1$ means neutral, $i = 2$ means singly ionized, and $i = Z + 1$ is the fully stripped ion with atomic number Z), n_e is the electron density, and $C(T_e)_i$ and $R(T_e)_i$ are the ionization and recombination rate coefficients for this ion. This equation represents a set of coupled equations. For example, there are $Z + 1$ ionization states and the same number of equations for each atom of atomic number Z . The ionization rate coefficient includes collisional and auto-ionization rate

³ <http://www.predsci.com/corona/jul10eclipse/jul10eclipse.html>

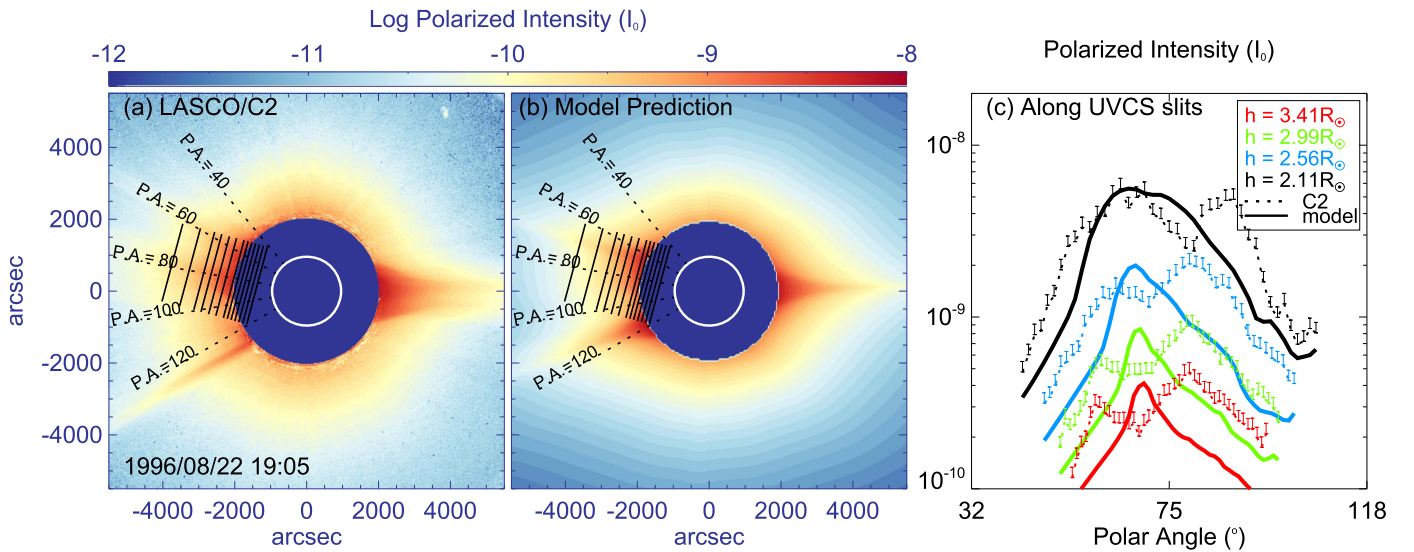


Figure 1. (a) LASCO C2 polarized intensity image with UVCS slit positions shown, (b) simulated polarized intensity from this model, and (c) intensity profiles along the UVCS slit direction at 1996 August 22 at 19:05 UT. The blue disks indicate the C2 occulter disk, and the white circles indicate the solar disk. In panels (a) and (b), the solid lines indicate the location of UVCS slits, and the dotted lines show the direction of different polar angle on the sky plane. In panel (c), dotted and solid lines are for C2 observations and model predictions at different heights. Here, I_0 is the polarized intensity in units of the mean of solar disk brightness.

coefficients, and the recombination rate includes radiative and dielectronic recombination rate coefficients, which strongly depend on the temperature but are not very sensitive to the electron density.

To solve the above equations, we need the evolutionary history of temperature and density of each cell of plasma in a Lagrangian framework. As in our previous paper (Shen et al. 2013), we find the evolutionary history for any position around a pseudostreamer. In the regions around this streamer, we define a group of cells on the 3D grid of the numerical calculations. For example, in order to compare our calculations with UVCS observations, we set $(13 \times 41 \times 295)$ sampling cells at 13 different heights where the UVCS slits are located, as shown in Figure 1. In Figure 1(a) and (b), we show the UVCS slits using straight solid lines on the LASCO C2 polarized intensity background. Panel (c) of Figure 1 shows polarized intensity profiles along these slits, which will be discussed in the following section. At each of these chosen heights, there are 41 cells along the UVCS slit and 295 nonuniform cells in the LOS direction. We then trace the path of the plasma parcel in each cell as it moves along the magnetic field line at the local plasma flow speed. Because the MAS model is a steady solution, this method of tracing is accurate. Thus for each plasma parcel, a trajectory that is connected back to the solar surface gives the temperature and density history in a Lagrangian framework.

Along each trajectory, the charge states are assumed to be in equilibrium at the solar surface, and the NEI states at later times are obtained by solving Equation (1). We calculate NEI states of several elements including H, O, Mg, Si, and Fe. The calculation code is based on the eigenvalue method of solving time-dependent ionization equations (Masai 1984; Hughes & Helfand 1985), but introduces an efficient adaptive time-step strategy to quickly perform the computations (see Shen et al. 2015a). We use ionization and recombination rate coefficients from Version 7 of CHIANTI (Landi et al. 2012), which are described by Dere (2007) and Dere et al. (2009). Therefore, for each position around this pseudostreamer in the

3D framework, we get the ion fractions of each element along the plasma trajectory that intersects that point.

3. Results

3.1. The Topology of this Pseudostreamer

This 3D MHD global simulation includes a distribution of open and closed magnetic structures, as well as current sheets representing the steady-state corona during the WSM. We identify regions in the photosphere with open magnetic field lines as coronal holes. Here, we focus on a pseudostreamer structure that is located on the northeastern limb on 1996 August 22, spanning roughly 55° to 75° in polar angle (P.A.), measured from the north toward the solar equator. It extends to several solar radii (see Figure 1(a)), and originates from a region at the surface within $\sim 250^\circ$ to $\sim 285^\circ$ in Carrington longitude and roughly -30° to $+60^\circ$ in Carrington latitude (see Figures 2 and 7). Flow through a temperature gradient can cause significant departures from equilibrium ionization in the open field regions of the pseudostreamer, while the ionization state could still be in equilibrium in the stationary, dense plasma in the closed field region. Therefore, it is important to analyze NEI states of the pseudostreamer in a 3D MHD corona model.

Panel (a) in Figure 2 shows the radial magnetic field at the solar surface for CR1913, and panel (b) shows the simulated coronal holes. The green rectangle indicates the region in which the pseudostreamer could be seen at the east limb of the Sun between August 20 and 23. The magnetic topology of this pseudostreamer is displayed in Figure 3, where we show several magnetic field lines and the radial field at the solar surface. This pseudostreamer can be identified from some converging red lines in the northern hemisphere. Red means the magnetic lines extend out from positive polarity regions. Because there are negative magnetic polarity regions inside this pseudostreamer, we also can clearly see two pairs of closed loops at the lower altitudes in the pseudostreamer. In order to understand the physical properties of this pseudostreamer, we also draw a plane that includes the UVCS slit and the

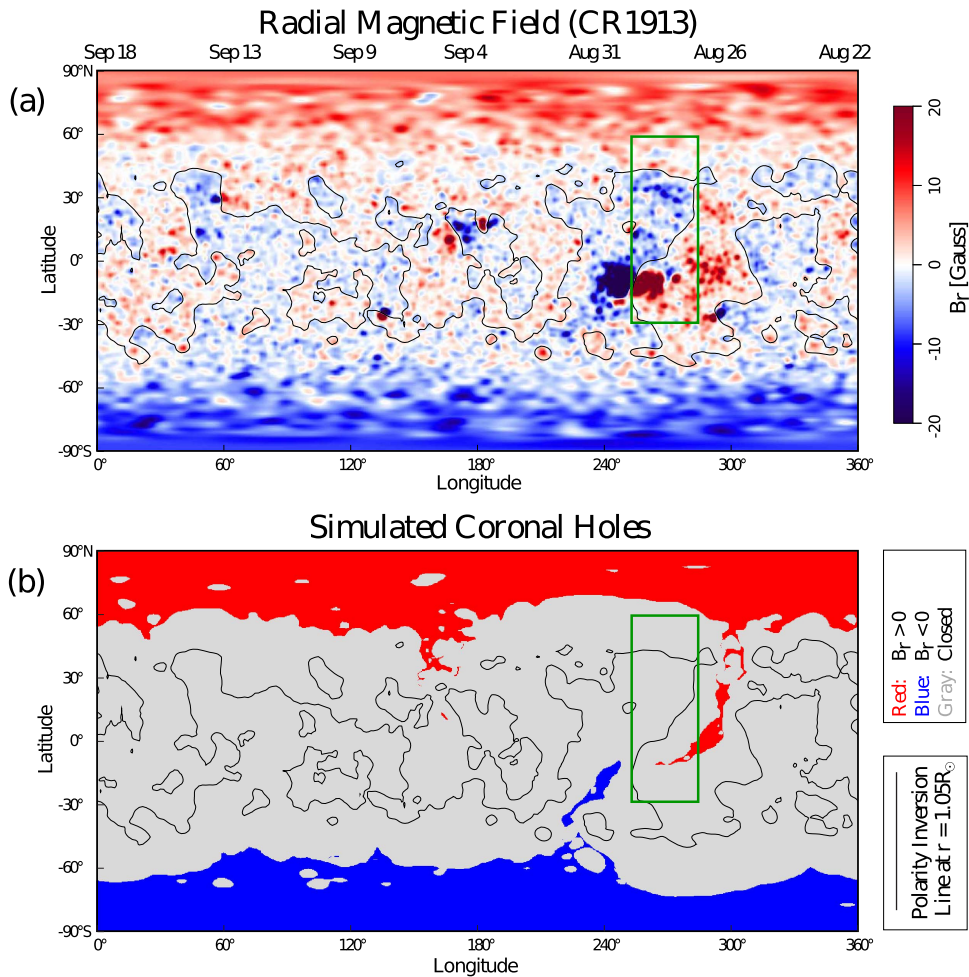


Figure 2. Magnetic field model for the Sun around the time of Whole Sun Month (Carrington Rotation 1913, 1996 August 22 to September 18). (a) The B_r component at 1.0 solar radii. The color bar is for B_r . (b) The simulated distribution of coronal holes (open-field regions). Here, red indicates $B_r > 0$, blue indicates $B_r < 0$, and gray is for closed regions. The green box indicates a pseudostreamer can be seen at the east limb of the Sun between August 20 to August 23, and the top and bottom edges of the green box indicate the latitude ranges covered by the UVCS slits.

LOS at heights (a) $h = 2.99 R_\odot$ and (b) $h = 2.00 R_\odot$ from Sun center, and we will discuss the ionization features on these planes in the following sections. In Figure 3, the colors of these chosen planes indicate the temperature distribution. The color along a magnetic field line indicates the sign of B_r , where red is for $B_r > 0$ and blue is for $B_r < 0$.

The *SOHO*/UVCS slit is positioned perpendicular to radial rays emanating from the center of the Sun (see Figure 1). Here, we use the polar angle (P.A.) of these radial rays to describe the position of the UVCS slits. The *SOHO*/UVCS slit is located at P.A. = 75° , and it covers the pseudostreamer at several heights so that we can compare the synthetic intensities with the UVCS spectral lines.

In Figure 1, we display a polarized intensity image from the observations of LASCO-C2 at 1996 August 22 19:05 UT and a predicted polarized intensity from this simulation. These polarized brightness images are obtained and calibrated by the SolarSoft (SSW) library (Freeland & Handy 1998). Because the current SSW library depends on an old LASCO calibration, the intensity shown in Figure 1(a) is smaller by around 15% than the actual intensity from recent studies of photometric calibration for LASCO-C2 (Gardès et al. 2013; Colaninno & Howard 2015). Because the polarization brightness emission is produced by the scattering by electrons in the solar corona and it depends on the integral of electron density along the LOS, the dense coronal

streamer structures can be seen as bright regions in these white-light images. We can make an observational prediction of polarized brightness (Billings 1966) from the electron density from the MHD simulations. In the region of the UVCS observations, comparison of the model with the LASCO image indicates that the model predicts too high a density in the area of the pseudostreamer (P.A. $\sim 60^\circ$, see dotted line in Figure 1) and too low a density around the streamer at P.A. $\sim 80^\circ$ which can be found in panel (c) of Figure 1. Figure 1(c) shows that the simulated density structure matches the observation on average, but fails to match the spatial structure, possibly due to contamination of structures along the LOS. This discrepancy is very likely to be caused by an inaccurate magnetic configuration at the lower boundary. Nevertheless, the overall level of the polarized brightness compares reasonably well with observations.

In order to analyze ionization features around this pseudostreamer, it is helpful to investigate the velocity distribution at different heights. In Figure 4, we show the simulated temperature, density, radial velocity, and radial magnetic field component distributions in selected planes at different heights. To compare with UVCS observations, we choose a set of heights where UVCS slits were located. In each panel of Figure 4, the vertical axis is the UVCS slit direction labeled by polar angle, and the horizontal axis is the LOS direction, so the brightness seen by

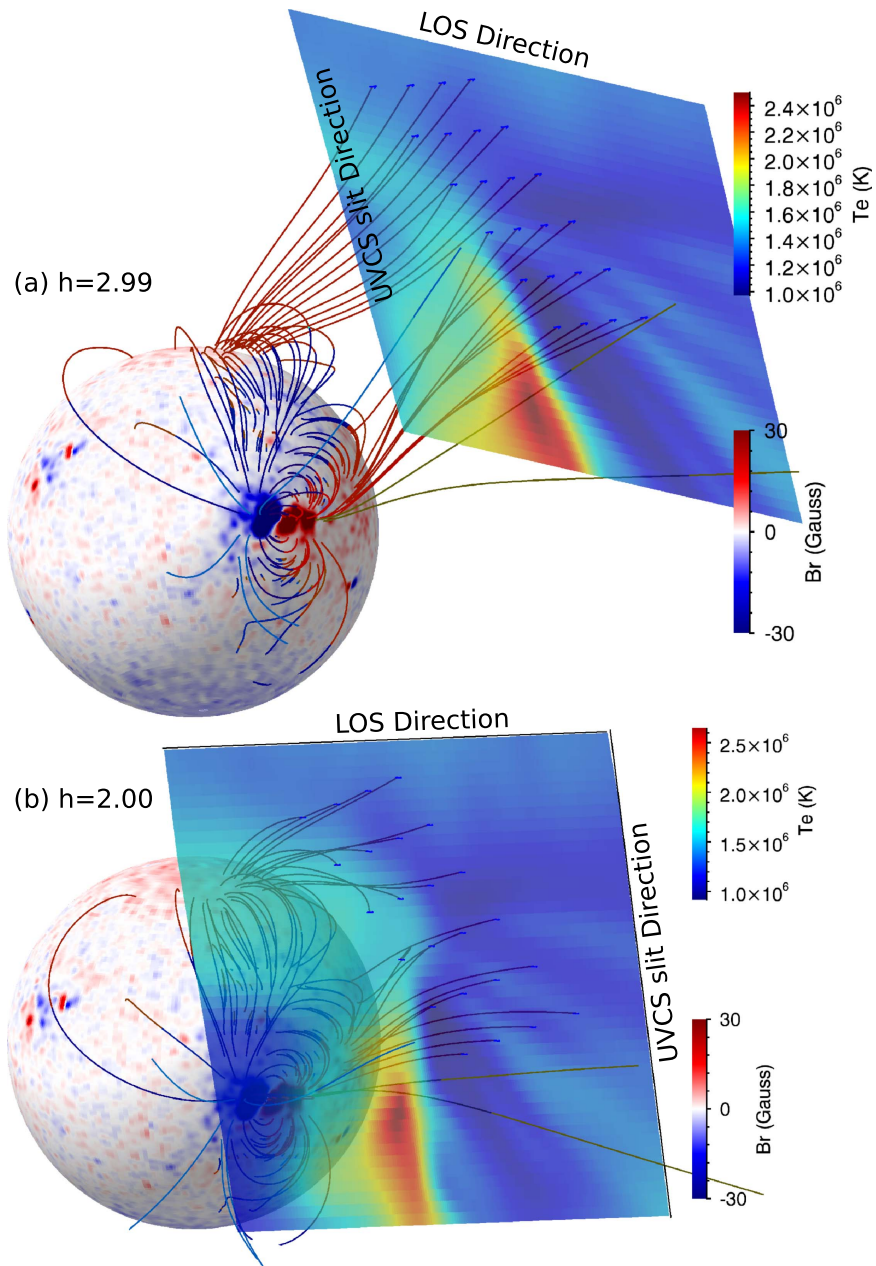


Figure 3. The radial magnetic field distribution projected on the solar surface and selected magnetic field lines from the MHD solution. The shadow planes indicate heights (a) $h = 2.99 R_{\odot}$ and (b) $h = 2.00 R_{\odot}$ where the UVCS slit is located, and the color of these planes indicates temperature distribution. The intersection of pseudostreamer magnetic field lines with these shadow planes are plotted as blue points on these planes. The color along a magnetic field line indicates the polarization of B_r , where red is for $B_r > 0$ and blue is for $B_r < 0$.

UVCS at any position along the slit is the integral of the emissivity along the LOS direction.

This pseudostreamer can be distinguished in these complex two-dimensional panels by using the boundary of coronal holes and the magnetic field polarity. For this purpose, we computed three-dimensional coronal hole boundaries by tracing field lines throughout the whole computational volume. We plot the coronal hole boundaries on each panel using solid lines. The center region between the two solid lines is one where magnetic field lines are closed; outside the two solid lines, the fields are open. Figure 3 shows that the magnetic polarity is negative in the center of this pseudostreamer at low altitude. Therefore, we can see that this pseudostreamer is located in the top-right

regions in Figure 4, where the magnetic polarity turns from positive outer regions at large height to a negative inner region at low heights. The “+” signs indicate crossing positions where the magnetic lines plotted in Figure 3 intersect the sampling planes. We can see that almost all “+” signs are located in the open field region of this pseudostreamer at high altitude ($h = 2.99 R_{\odot}$), and more “+” signs are located inside the closed field region at lower height ($h = 2.00 R_{\odot}$).

As the height increases from $h = 1.41 R_{\odot}$ to $h = 2.99 R_{\odot}$, we can clearly see this pseudostreamer. In open magnetic field regions at large height ($h = 2.99 R_{\odot}$), the center part of this pseudostreamer has lower outflow speed, lower temperature, and higher density than the ambient open field regions. The

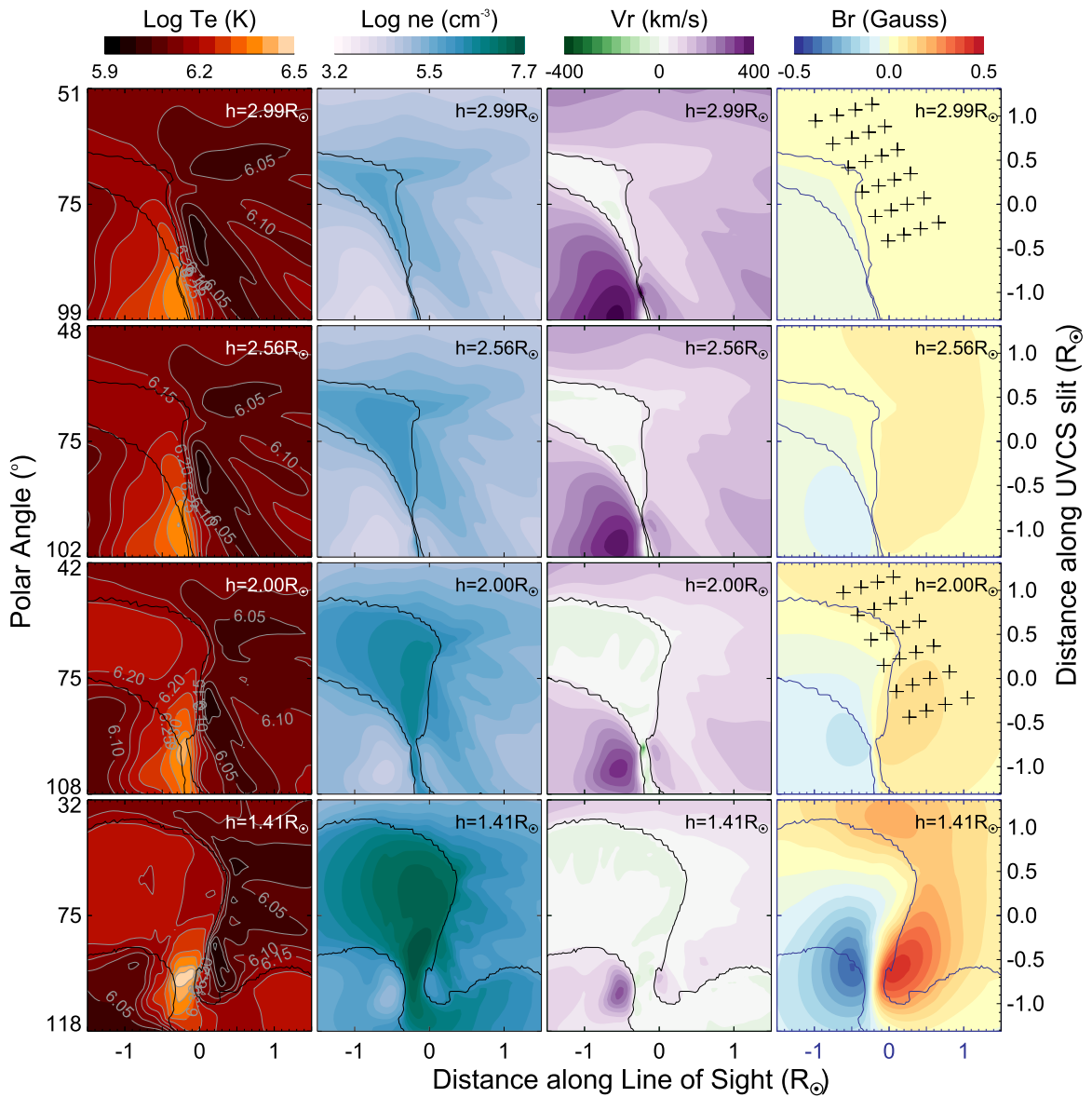


Figure 4. Temperature, density, radial velocity component, and radial magnetic field are shown at different UVCS slit heights from $h = 1.41, 2.00, 2.56 R_{\odot}$ to $h = 2.99 R_{\odot}$. Each row indicates a height in this plotting. The coronal hole boundary is shown by the solid lines. The region within this contour has closed field lines, with open field lines outside coronal holes. The intersections of pseudostreamer magnetic field lines with these shadow planes in Figure 2 are noted as “+” signs.

outflow speeds are lower in the pseudostreamer center than ambient regions, but increase with height. The maximum speed is close to 150 km s^{-1} at the $h = 2.99 R_{\odot}$ plane and polar angle P.A. = 60° . At low height ($h = 1.41 R_{\odot}$), we can see more closed field regions of this pseudostreamer. The center temperature is as low as $\sim 10^6 \text{ K}$, while the maximum temperature appears in the closed field region. The closed magnetic loops have a strong effect on density at both high altitude and low altitude, and the density in closed field regions is higher than the ambient open field regions as well. Slow flows of several to tens of km s^{-1} can be found inside closed regions, which are systematic siphon-like flows (Reale 2014). Because the sampling planes are also close to an active region located in the left-bottom corner, we also can see high temperature, velocity, and density. There is a streamer farther to the south along the UVCS slit (near P.A. = 90°), with temperatures reaching $10^{6.4} \text{ K}$, with higher densities and higher outflow speeds than in the pseudostreamer.

3.2. Ionization Features

In this section, we calculate distributions of ionic charge states in the pseudostreamer and surrounding regions at 13 different heights (1.41, 1.53, 1.65, 1.77, 1.88, 2.00, 2.11, 2.33, 2.56, 2.78, 2.99, 3.41, and $3.93 R_{\odot}$), and show how the NEI state changes at different heights and regions. We show the ionization fraction distributions of several ions at different heights in Figure 5, including H I (neutral hydrogen), O VI (O^{+5}), Mg X (Mg^{+9}), Si XII (Si^{+11}), and Fe XII (Fe^{+11}).

Hydrogen is almost fully ionized in the coronal environment, and the maximum of H I fraction decreases slightly with increasing height. As the height increases to $h = 2.56 R_{\odot}$, the maximum H I fraction decreases to 2.82×10^{-7} from 3.18×10^{-7} at $h = 1.41 R_{\odot}$. For O VI, the maximum fraction at all heights is lower than around 0.1 because the temperature is high enough that the dominant oxygen ion is O VII. The maximum O VI only appears at the high polar angle end, P.A. = 102° , where the temperature drops from around $10^{6.2} \text{ K}$

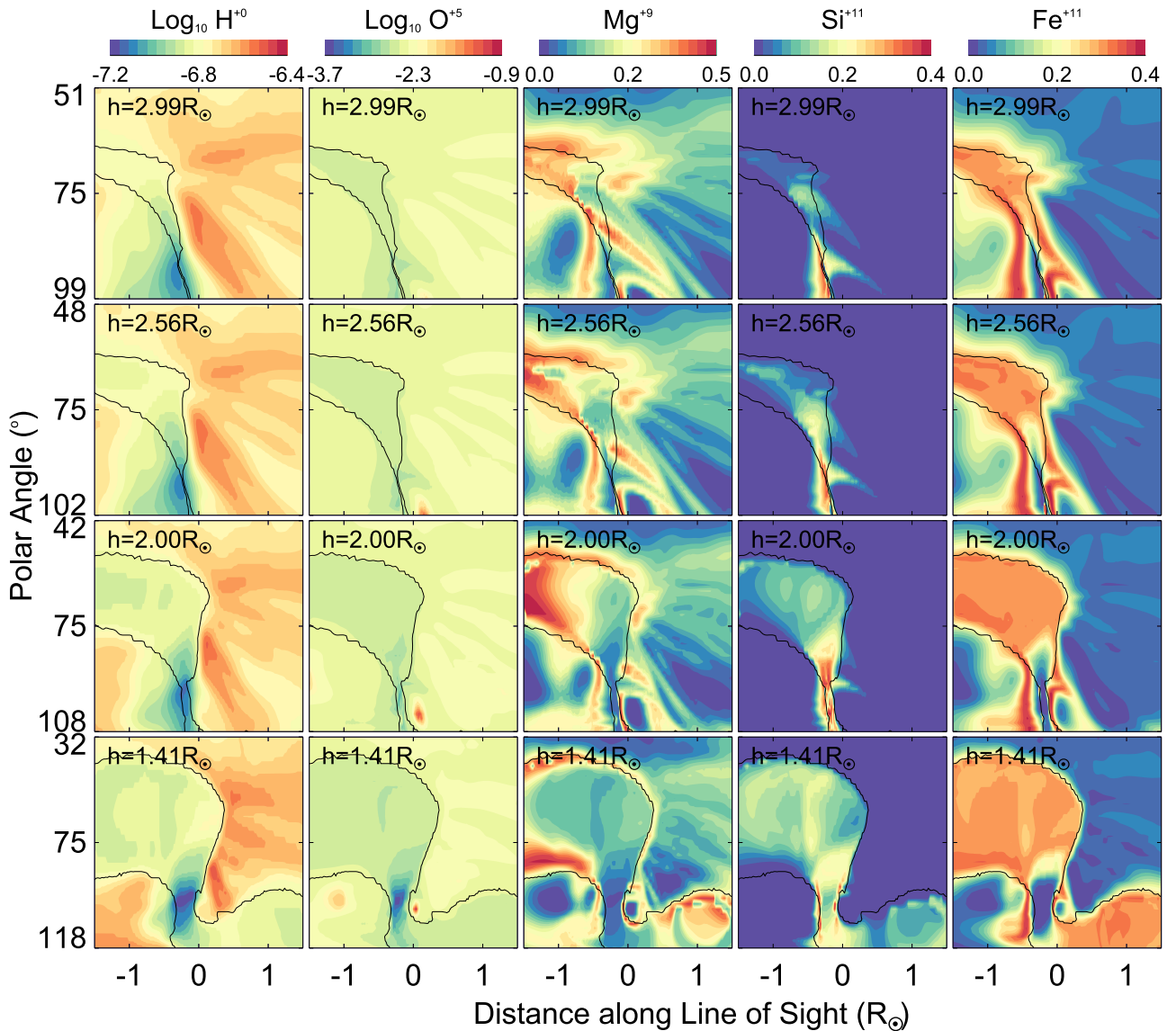


Figure 5. Ionic charge fractions of several ions at different heights.

to the coronal hole value of $10^{6.0}$ K, and the outflow velocity is significantly larger than in the pseudostreamer. The populations of Mg X, Si XII, and Fe XII are significant at all these heights. The largest amount of Mg X appears at coronal hole boundaries at low altitudes, and there are enhancements around the pseudostreamer at high altitude. The Si XII and Fe XII ions are most abundant in a low closed-field region. As the height increases, more Si XII and Fe XII ions also appear in the open field regions around this pseudostreamer.

To compare the results of NEI with the equilibrium assumption, we plot the relative difference of ion populations between the two cases in Figure 6. Because the ion fraction can be very tiny under either the non-equilibrium or equilibrium, we define the relative difference as:

$$f_{\text{diff}} = \frac{f_{\text{nei}} - f_{\text{ei}}}{f_{\text{nei}} + f_{\text{ei}}}. \quad (2)$$

Here, nei stands for NEI, ei stands for equilibrium ionization, f_{nei} is the ion fraction of time-dependent ionization calculations, and f_{ei} is for equilibrium ionization assumption. When the

relative difference, f_{diff} , is close to +1, this indicates that the equilibrium ion fraction is tiny and the non-equilibrium ion fraction is many times higher, and vice versa for $f_{\text{diff}} = -1$. While this is a convenient way to show departures in either direction, it is a compressed scale. For instance, $f_{\text{diff}} = 0.9$ means that $f_{\text{nei}} = 19f_{\text{ei}}$. We use sienna color to display the location where the relative difference is close to zero, for example: $|f_{\text{diff}}| < 0.03$ in Figure 6. For neutral hydrogen, because the coronal electron density continues to decrease with height, the effect of NEI becomes apparent at the higher altitudes. In Figure 6, we can see that the relative difference of H I between the two cases increases slightly as the height increases, and the maximum difference is 0.073 at $h = 2.99 R_{\odot}$. This is a modest change because the ionization rate of H I is very large. We also can see that the relative difference of H I does correlate with the shape of the pseudostreamer.

For other ions, such as O VI, Mg X, Si XII, and Fe XII, the ion fraction difference can be large. For O VI, the maximum

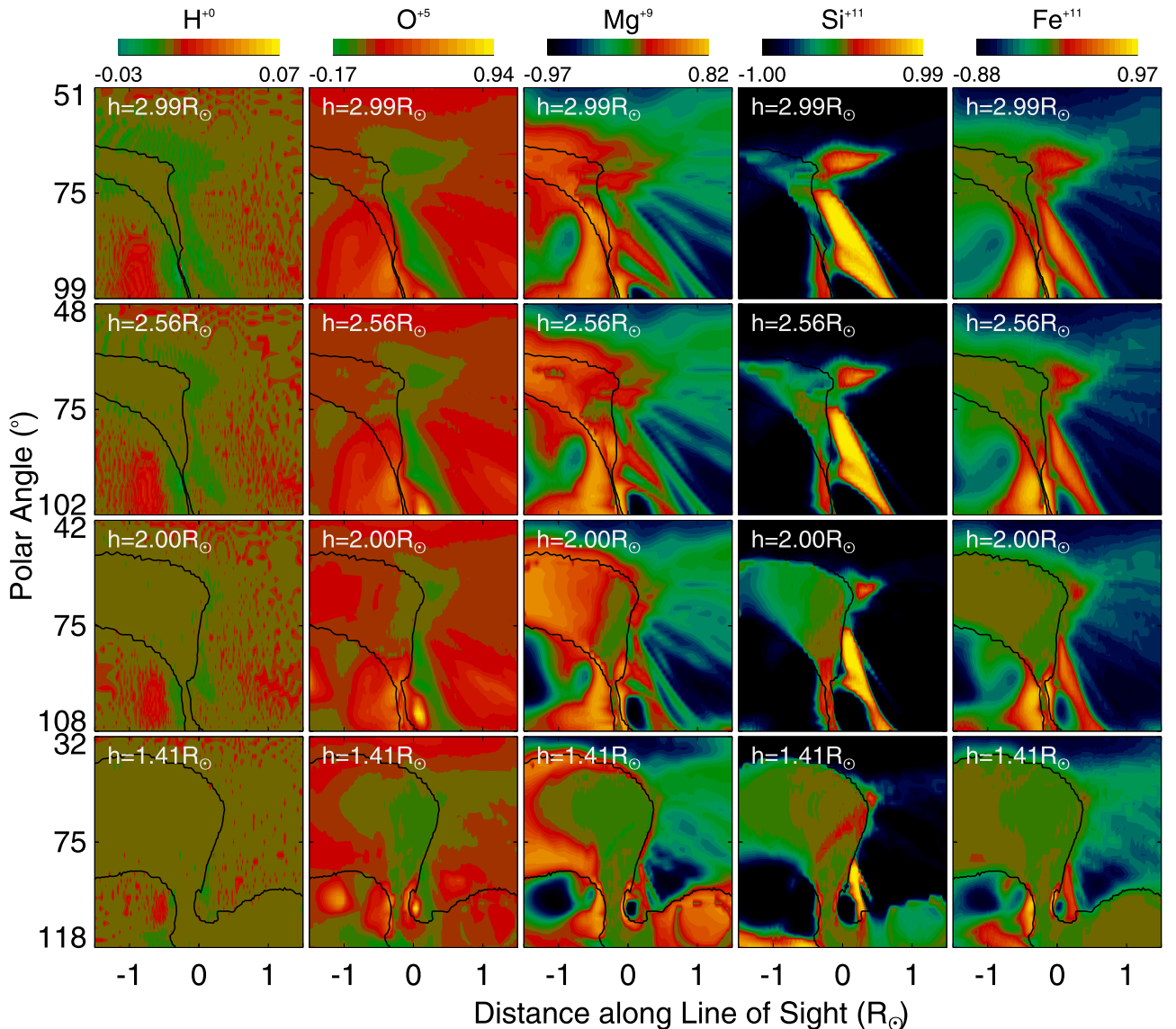


Figure 6. Ionic charge fraction relative difference f_{diff} between non-equilibrium and equilibrium ionization. Sienna-colored regions show the position where $-0.002 < f_{\text{diff}} < 0.002$ for H I ions and $-0.03 < f_{\text{diff}} < 0.03$ for O VI, Mg X, Si XII, and Fe XII. The white solid lines indicate the boundary of coronal holes.

difference is close to 0.94 in high outflow regions, while a slightly negative difference appears in the slow flow region of this pseudostreamer where electron density is higher and outflows are slower than in the ambient region. At low altitude ($h = 1.41 R_{\odot}$), the smallest relative difference regions (sienna color) are contained within the closed field boundary for Mg X, Si XII, and Fe XII, where the magnetic lines are closed and the velocity is low, such that the plasma will be close to ionization equilibrium. However, ionization states still have slight departures from ionization equilibrium states in closed regions due to the systematic siphon-like flow. For example, Mg X is still clearly enhanced even within closed field regions at all altitudes. At higher altitude ($h > 2.0 R_{\odot}$), the Mg X, Si XII, and Fe XII fractions are enhanced in the NEI case compared to the equilibrium assumption in the region around the streamer.

3.3. Charge States in Center of Pseudostreamer

Because the charge states around a structure can be compared to typical measured values of frozen in charge states in situ (Zurbuchen et al. 2002), we show here the average

oxygen ion fractions at $3.93 R_{\odot}$ in Figure 7. In Figure 7, we choose a set of sampling points on open field lines in the pseudostreamer and show ionic fractions of several oxygen ions along them. The plasma density is lower than $\sim 10^5 \text{ cm}^{-3}$, and the ionization state is close to frozen-in. As shown in Figure 7(a), we choose some points (“+”) in the center area of this pseudostreamer with low radial velocity ($v_r < 180 \text{ km s}^{-1}$) and relative difference ($f_{\text{diff}} \text{ O}^{5+} < -0.02$) between NEI and equilibrium ionization (EI) cases. These sampling points have been traced backward to the solar surface, $r = 1.02 R_{\odot}$, along magnetic lines. In Figure 7(b), we can see that these chosen points indeed come from two separate magnetic positive polarity foot-points regions. The results are shown in Figure 7(c). The dominant oxygen ion is O VII (O^{6+}) with a population above 98% in both NEI and EI cases. On the other hand, the oxygen is over-ionized, with the NEI fraction larger than EI for O VIII and smaller for O VI. The average relative differences for O VIII and O VI between NEI and equilibrium ionization are around 0.15 and 0.06, respectively. The error bars show the rms deviations from the averages. They show

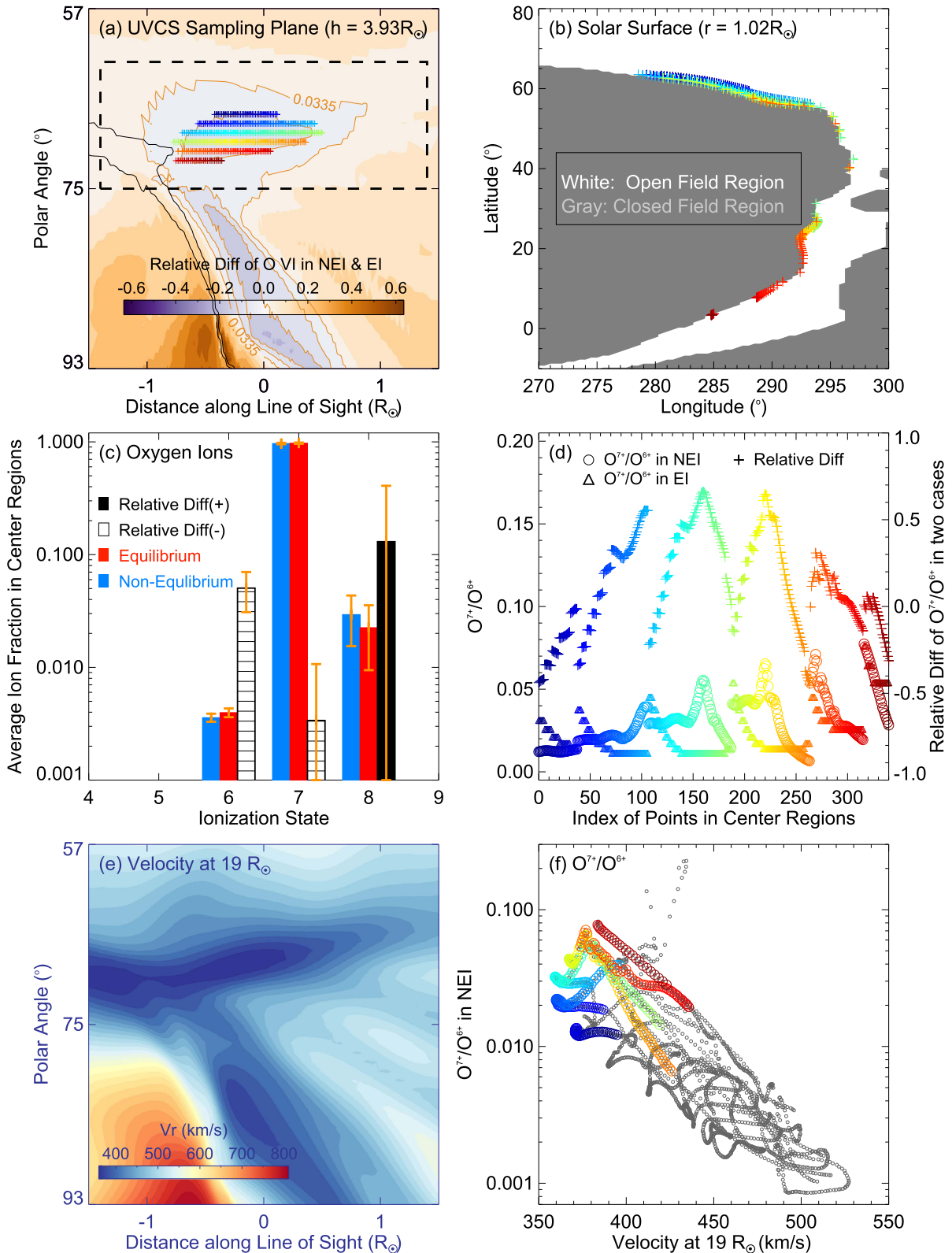


Figure 7. Average of ionic fractions in open field regions of this pseudostreamer at $h = 3.93 R_{\odot}$. (a) Relative difference of O VI ions between NEI and equilibrium ionization cases, as shown in Figure 6, and “+” signs indicate the chosen points near the low flow-speed center of this pseudostreamer in open regions. (b) The coronal hole boundary at the solar surface ($r = 1.02 R_{\odot}$). The “+” signs indicate the positions of chosen points that have been traced back to the solar surface from panel (a). (c) The average oxygen ion fraction for above chosen points. The white bar is for negative values and black is for positive values. Error bars show the standard deviations. (d) O^{7+}/O^{6+} ratio and the relative difference of O^{7+}/O^{6+} ratio in NEI and equilibrium ionization cases for above chosen points. (e) The final velocity distribution at $r = 19 R_{\odot}$ for the sampling plane at $h = 3.93 R_{\odot}$ shown on panel (a). (f) O^{7+}/O^{6+} ratios vs. velocity for sampling points in panel (a). The color circles indicate the same points chosen from panel (a) and gray circles are for others inside the dashed rectangle.

typical differences around 0.4 for O VIII and 0.1 for O VI. Thus, the effects of NEI on the O^{7+}/O^{6+} ratio are substantial in this region, but they tend to average out. The O^{7+}/O^{6+} ratio is not sensitive to conditions above the freeze-in point, but it is a clear prediction that we compare with in situ observations below. For instance, the O^{7+}/O^{6+} ratio is used extensively by the community to diagnose the solar wind source in low corona. It has been reported that periods of $O^{7+}/O^{6+} < 0.1$ are associated with coronal hole solar wind (von Steiger et al. 2001; Zurbuchen et al. 2002), and a number of time periods with $O^{7+}/O^{6+} > 1.0$ are typically associated with coronal mass ejections (Lepri et al. 2001; Henke et al. 2001). Figure 7(d) shows the O^{7+}/O^{6+} ratio and the relative difference of O^{7+}/O^{6+} ratio between NEI and EI cases for the sampling points in panel (a), with corresponding colors. This figure shows that the O^{7+}/O^{6+} ratio ranges from ~ 0.01 to ~ 0.08 in center regions of this pseudostreamer because the center region of this pseudostreamer is cool (~ 1.1 MK). In NEI cases, the O^{7+}/O^{6+} ratio can be larger (or less) than equilibrium cases. However, the O^{7+}/O^{6+} ratio depends strongly on spatial position. Along each line in constant position angle in panel (a), there is a coherent trend as the relative difference of O^{7+}/O^{6+} ratio swings from negative to positive and back to negative, with values corresponding to differences in the O^{7+} ionization fraction as large as a factor of 4.5.

To further improve our understanding about how ratios of O^{7+}/O^{6+} change with velocity, we calculate the O^{7+}/O^{6+} ratio in extension regions around this pseudostreamer. We choose sampling points from a larger zone as shown from the dashed box in Figure 7(a), and compute O^{7+}/O^{6+} ratio on these points within open field regions. Figure 7(e) displays the terminal solar wind velocities achieved by the sampling points, extracted at $r = 19 R_{\odot}$, and Figure 7(f) plots the corresponding O^{7+}/O^{6+} ratio. The color circles mark the center regions of the pseudostreamer as shown in panels (a), (b), and (d). In Figure 7(e), we plot the plasma speed at $r = 19 R_{\odot}$ by tracing the flows from this sampling plane ($h = 3.93 R_{\odot}$) to higher altitudes. The minimum velocity in central regions of this pseudostreamer is ~ 350 km s $^{-1}$, as the plasma moves upward to $r = 19 R_{\odot}$. In Figure 7(f), the overall feature is that O^{7+}/O^{6+} ratios increase as the velocity decreases. At the lower velocity (~ 350 km s $^{-1}$) end, O^{7+}/O^{6+} ratios can reach ~ 0.08 in the pseudostreamer center. Although the ratio also varies at the low-velocity end due to the temperature variation, the color circles also indicate that the pseudostreamer has a higher O^{7+}/O^{6+} ratio than the surrounding open field regions. Abbo et al. (2015) reported a higher O^{7+}/O^{6+} ratio (around 0.2) in pseudostreamer regions as opposed to other open field lines. Our ratio in the pseudostreamer is smaller, which is probably due to the cool temperature in our model. Cranmer (2014) examined O^{7+}/O^{6+} ratios as a function of wind speed at 1 au, and found that the superthermal electrons can enhance the charge states of oxygen ions. The ratio shown in Figure 7(f) are less than values from Cranmer (2014). However, Figure 7(f) plots the ratio in the lower-velocity range (~ 350 to ~ 550 km s $^{-1}$).

3.4. Predicted Intensity

To predict intensity profiles along the UVCS slit and compare them to UVCS observations, we make the above time-dependent ionization calculations for H I, O VI, Mg X, and Si XII, and calculate synthetic Ly α , O VI 1032/1037 Å, Mg X

610 Å, and Si XII 499/521 Å line intensities. For each ion, the line emissivities are calculated at the chosen height in the plane including the LOS and the UVCS slit. For each ion of a given element, the optical thin line emission is calculated by the formula:

$$I_{\text{line}} = \frac{n_x}{4\pi n_H} \int G(T_e) dEM(T_e), \quad (3)$$

where I_{line} is in units of photon cm $^{-2}$ s $^{-1}$ sr $^{-1}$, and n_x/n_H is the elemental abundance based on the coronal values in the CHIANTI atomic database (Landi et al. 2013). We use coronal abundance data described by Schmelz et al. (2012) in the following calculations. Here, G is the contribution function that is calculated by using the emissivities calculated from CHIANTI (version 7; Landi et al. 2012) and the ionic fraction of NEI results in NEI cases (or equilibrium ionic fraction in EI cases). The differential emission measure, which depends on n_e and LOS length, is shown as dEM . Then the emissivities are integrated along LOS for about $15 R_{\odot}$ in this work.

For the Ly α , O VI 1032/1037 Å lines, we include the intensity of solar disk emission line photons resonantly scattered into the LOS, which depends on the outflow speed and line width (e.g., Withbroe 1982; Noci et al. 1987). In computing the scattered emission, we use the temperature given by the MHD model for the line widths, though the actual line widths are likely to be larger, especially at the larger heights (Strachan et al. 2002; Frazin et al. 2003; Abbo et al. 2015). We measure Ly α line widths about 1.5 times the thermal width and O VI widths ranging from 1.5 times the thermal width at low heights, up to four times the thermal width higher up. The scattered intensity is given by the convolution of the emission line profile from the disk and the scattering profile, so it depends on both the outflow speed and the line width. The scattered intensity of Ly α is not strongly affected by the larger line widths because the chromospheric line is very broad. The scattered O VI intensity is slightly reduced at low heights, but somewhat enhanced at larger heights because the Doppler dimming is less severe. UVCS observed intensities include a contribution from stray light that is modest at Coronal Hole intensities (Cranmer et al. 2010) and correspondingly less significant in the brighter regions observed here, so we have not corrected for it.

Figure 8 shows predicted intensity images from the MHD model and observed line intensity profiles at $h = 1.41 R_{\odot}$. The left column shows synthetic emissivities from NEI calculations in a plane containing the UVCS slit and the LOS, the middle column shows the predicted intensity profile calculated from different flow speed intervals in the sampling plane, and the right column shows both the predicted and observed intensity profiles along UVCS slits. For Ly α and O VI 1032/1037 Å, the ion fraction in the NEI case is relatively small around this pseudostreamer, and the scattering intensity also strongly depends on electron density and plasma outflow speed; therefore, the intensity distribution is strongly affected by electron density. Comparing the predicted UVCS profiles with the observations, we can see the simulated Ly α , O VI 1032/1037 Å, and Mg X 610 Å lines match the observation well at $h = 1.41 R_{\odot}$, except the slight dislocation along the polar angle direction. For Mg X 610 Å, there are some intensity differences around polar angle 61°. For Si XII 499/521 Å lines, the predicted intensity is too large around polar angle 85°. We

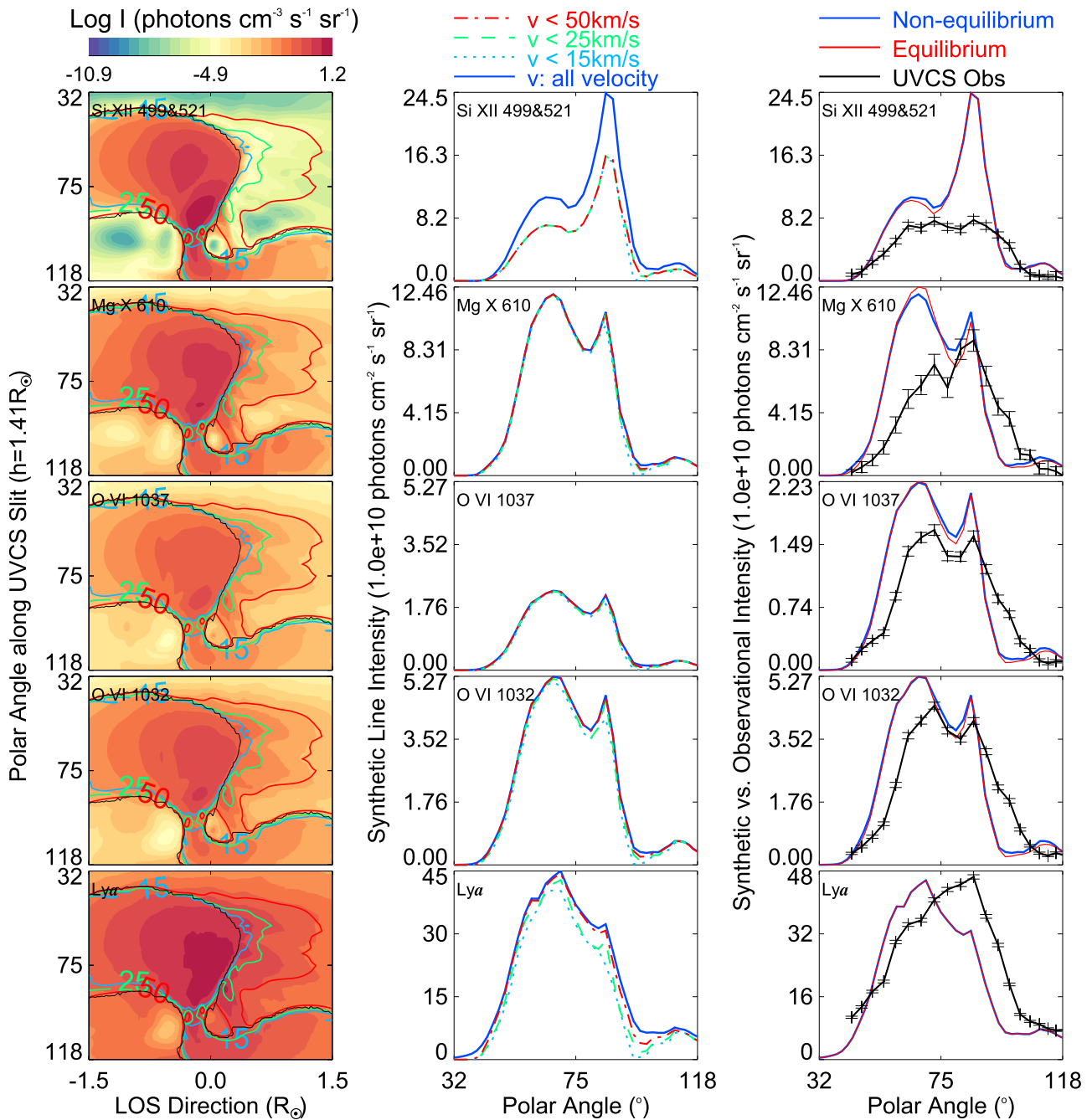


Figure 8. Left: synthetic line intensity distribution from this model at height $h = 1.41 R_{\odot}$. The black line indicates the coronal hole boundary, and color contour lines show different plasma flow speed, 15, 25, and 50 km s^{-1} . We show here the total intensity of Si XII 499 and 521 \AA to increase the signal-to-noise. Middle: model predicted line intensity profiles calculated from different speed regions. The blue lines are obtained through the whole sampling plane, the cyan, green, and red lines are computed by integrating synthetic intensities inside a corresponding lower speed region around this pseudostreamer. Right: Predicted line intensity profiles vs. *SOHO*/UVCS observations at 1996 August 21 20:08UT. The error-bars show statistical errors, including errors in the background level, and all observational lines from UVCS are shown here after performing data binning with bin size of 2.

will discuss possible reasons for the discrepancy between predicted and observational intensity at the end of this section.

Because synthetic intensity profiles along UVCS slits are integrations along the LOS, we also show the relative emission intensity contributions of the pseudostreamer and surrounding plasma in the middle column panels of Figure 8. The cyan, green, and red lines are integrated intensity profiles for NEI cases inside a low plasma flow-speed region, $v < 15$, $v < 25$, and $v < 50 \text{ km s}^{-1}$, and the blue lines cover all velocities.

Nearly all of the gas along the LOS outside the pseudostreamer is at $v > 50 \text{ km s}^{-1}$. It is clear that the difference between blue, red, green, and cyan lines is very tiny for Ly α , O VI 1032/1037 \AA , and Mg X 610 \AA lines. This indicates that the synthetic intensity along the LOS is dominated by the pseudostreamer for these lines, and the impact of emissions from outside regions is slight. For Si XII 499/521 \AA lines, the synthetic intensity from pseudostreamer and surrounding region (e.g., $v < 50 \text{ km s}^{-1}$) is lower than the integration on the whole sampling plane by up to

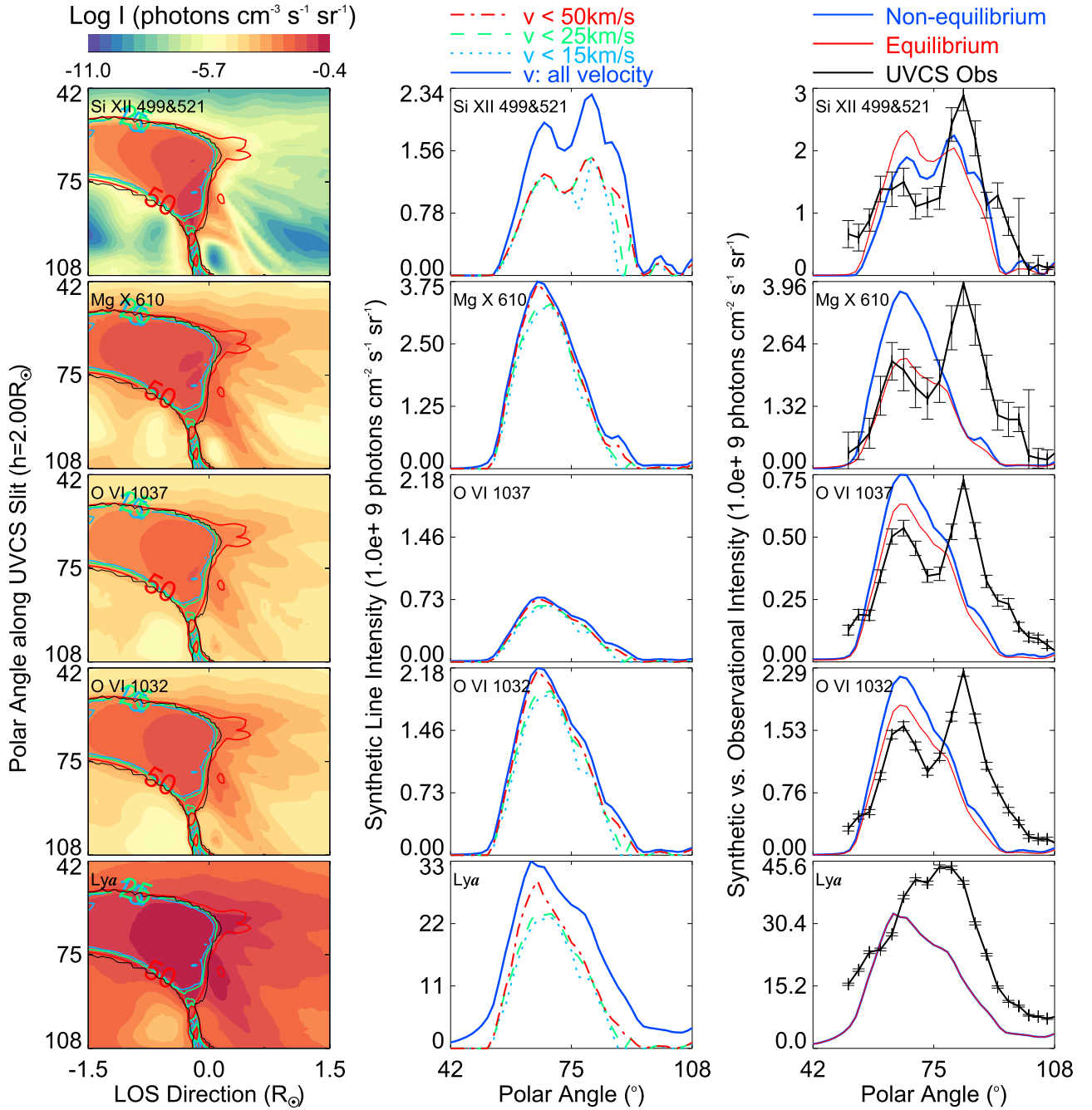


Figure 9. Same as Figure 8, except $h = 2.00 R_{\odot}$.

33%. However, the locations of the intensity peaks are same, and the predicted intensity profile shapes are similar.

The results at higher altitudes are shown in Figures 9 and 10, $h = 2.00 R_{\odot}$ and $h = 2.56 R_{\odot}$. The predicted $\text{Ly}\alpha$ intensity peak for the pseudostreamer clearly shifts to the low polar angle end and the profile becomes more narrow. For O VI 1032 Å, the predicted intensities from NEI calculations are modestly higher than under the ionization equilibrium assumption. Most strikingly, the observed lines show a strong enhancement at polar angle P.A. = 84° , which is barely visible in either equilibrium or non-equilibrium predictions. In the pseudostreamer region, the peak shifts to polar angle below 60° , and the NEI predictions are somewhat better than the EI predictions for Si XII and worse for Mg X.

For the Si XII lines, the NEI predicts weaker intensity than the equilibrium case. Comparing the Si XII prediction with UVCS observation profiles, the location of intensity peak still shifts to the low polar angle side.

To study where the NEI strongly affects the emission around this pseudostreamer, we use a quantity similar to the relative difference of ion fraction f_{diff} defined above, defining I_{diff} as

$$I_{\text{diff}} = (I_{\text{nei}} - I_{\text{ei}}) / (I_{\text{nei}} + I_{\text{ei}}), \quad (4)$$

where I_{nei} is the emission intensity for time-dependent ionization calculations, and I_{ei} represents the equilibrium ionization results, respectively. The relative difference I_{diff}

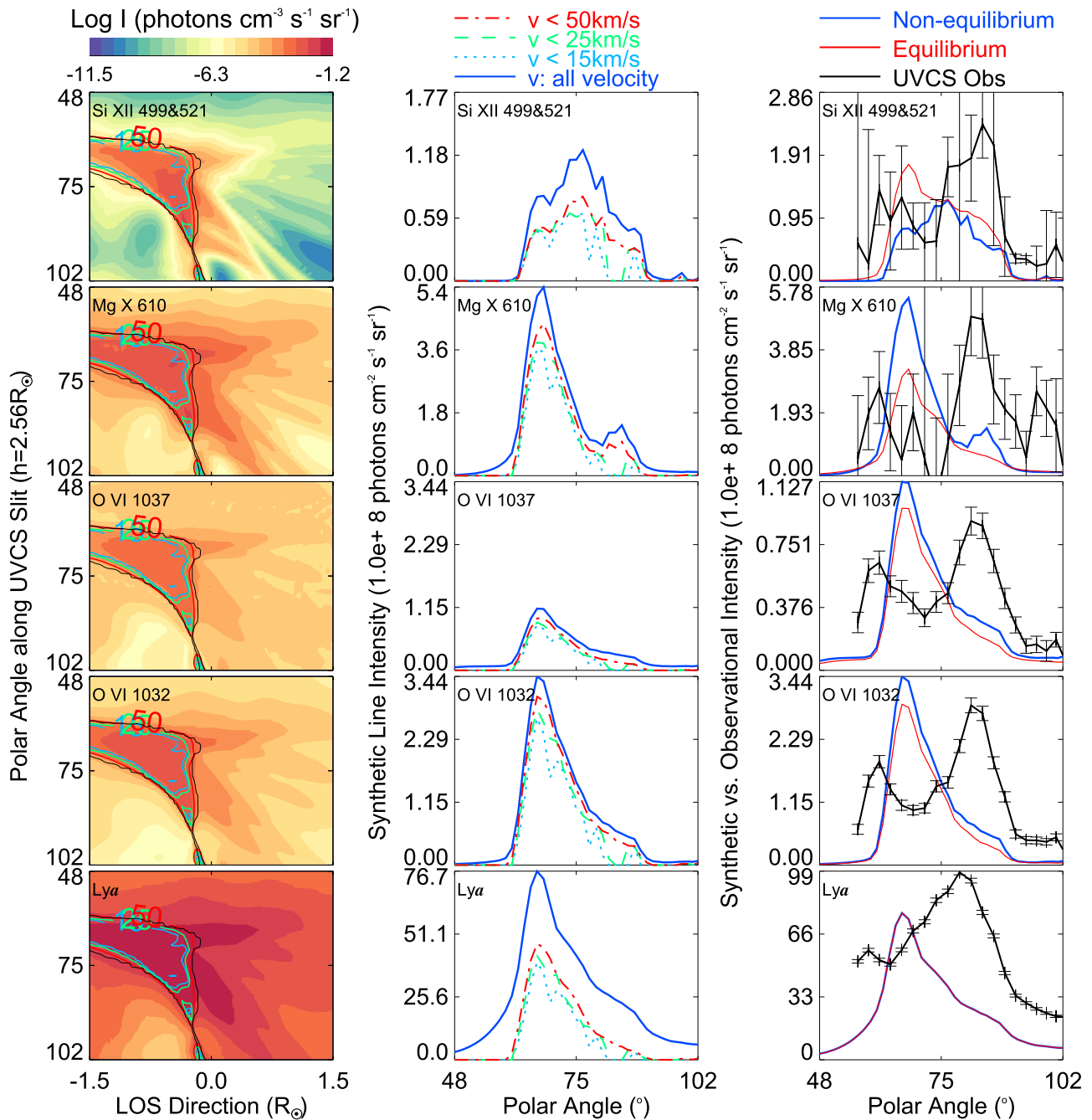


Figure 10. Same as Figure 8, except $h = 2.56 R_{\odot}$.

indicates the degree to which the intensity deviates from the equilibrium ionization assumption. Because the electron density and temperatures distributions are from the same MHD model for both non-equilibrium and equilibrium ionization cases, the predicted line emissivity only varies with ion fractions. Therefore, I_{diff} distributions are equivalent to the f_{diff} distributions shown in Figure 6.

We then can deduce how I_{diff} should vary with height from Figure 6. For $\text{Ly}\alpha$ and $\text{O } 1032 \text{ \AA}$, I_{diff} is positive in the region where outflow speed is highest, which means higher intensities in the non-equilibrium case. On the other hand, I_{diff} is near zero in the slow outflow region, which is not surprising because the ionization tends toward equilibrium in regions of low plasma

velocity. In addition, there are negative I_{diff} regions where the velocity and density are higher but temperature is lower. For $\text{Mg X } 610 \text{ \AA}$ and $\text{Si XII } 499 \text{ \AA}$, I_{diff} is large in the low-velocity and low-temperature region of this pseudostreamer at higher altitude, while it is negative in other regions.

We also display the difference of predicted UVCS intensity profiles between non-equilibrium and equilibrium ionization in Figure 11. The relative differences of UVCS intensities are less than 0.005 for $\text{Ly}\alpha$, ranging from -0.01 to 0.35 , roughly two times larger than the equilibrium assumption for $\text{O VI } 1032 \text{ \AA}$. For $\text{Mg } 610 \text{ \AA}$ and $\text{Si } 499/521 \text{ \AA}$, we also see that the relative differences of UVCS intensities are smaller than the maximum (or minimum) values in Figure 6. These differences occur

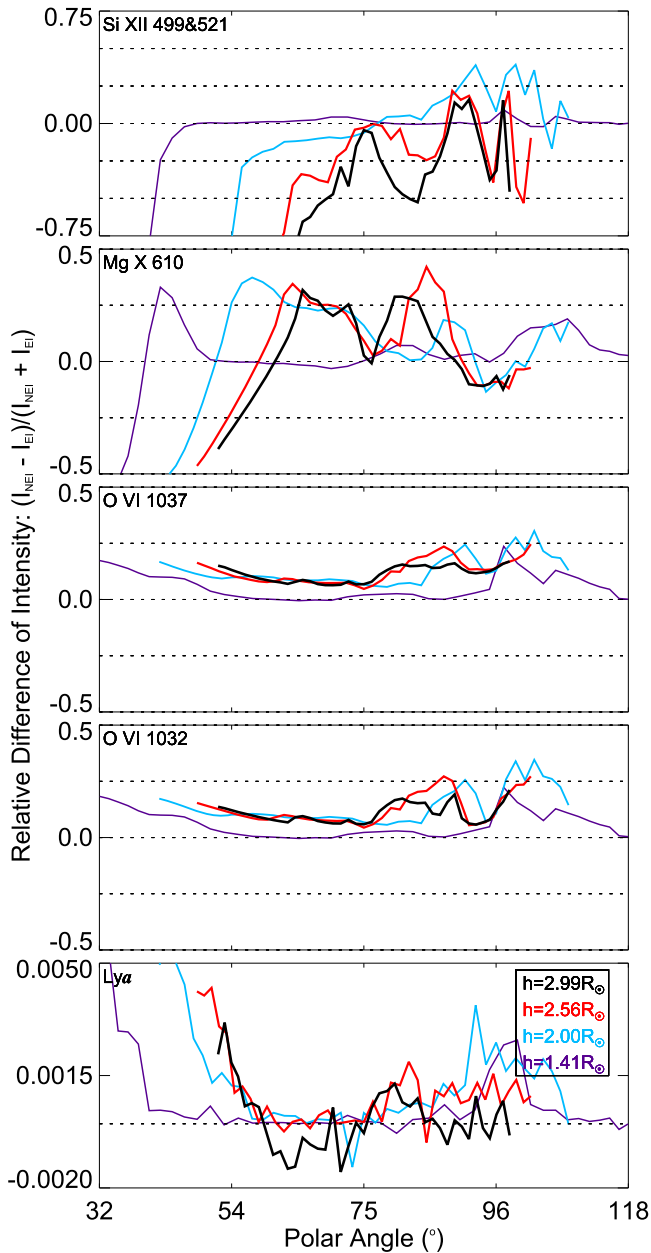


Figure 11. Relative difference of predicted UVCS intensity between non-equilibrium ionization (NEI) and equilibrium ionization (EI). The color indicates different UVCS heights from $h = 1.41, 2.00, 2.56, \text{ to } 2.99 R_{\odot}$.

because the UVCS intensities average out in many cases along the LOS direction, and the UVCS intensities are often dominated by dense regions where the departures from ionization equilibrium are smallest. Exactly how these the contributions from the different regions play out depends on the variation of elemental abundances between open and closed field regions due to the FIP effect and gravitational settling.

There are several assumptions in the model that could strongly affect the comparison to observations. First, the elemental abundances used in the emission calculations are taken to be same everywhere. However, stable closed magnetic loop systems often show severely depleted abundances due to gravitational settling (Raymond et al. 1997), so the contribution of static, dense regions close to ionization equilibrium may be badly overestimated. In the present case, most of the closed field region lies below the UVCS slit heights, but the closed

regions make a significant contribution to the predicted intensities at lower slit heights. There may also be variations in the abundances of low First Ionization Potential (FIP) elements between open and closed field regions, with low FIP elements being more abundant in closed loops (Laming et al. 1999; Ko et al. 2002; Feldman & Widing 2003). Second, we assume a filling factor of unity, while eclipse observations in white light (November & Koutchmy 1996) and observations of Comet C/2011 (Lovejoy) show a highly structured corona with magnetic flux tubes separated by a few thousand km that have density contrasts of order 6 (Raymond et al. 2014). Because the denser features dominate the emission, the spectrum will be closer to equilibrium than predicted by the models. It is not clear whether the high- or low-density flux tubes contribute more to the solar wind—and therefore the ion charge distributions measured at 1 au—but the low-density flux tubes would be further from equilibrium and the high-density ones closer. Third, we are using a single fluid model and therefore cannot treat differences among the proton, electron, and ion kinetic temperatures. If the electron temperature differs from the proton temperature, or if the electron velocity distribution has a non-thermal tail, that will directly affect the ionization balance. If different ions have different flow speeds, that will alter the relative abundances and the departure from equilibrium. For instance, Ofman et al. (2013) found that Mg X ions move more slowly than protons by up to about 20% in a multi-fluid model driven by Alfvén waves. In addition, if the kinetic temperature of oxygen differs from that of the protons, as observed, for instance, by Abbo et al. (2015), that will affect the radiative scattering contributions to the O VI lines and therefore the doublet ratio.

It is not really possible to make a direct, detailed comparison of our NEI calculations to other models, both because no other models considered this particular pseudostreamer structure and because few show results for this part of the corona in a form suitable for comparison. Moreover, each of the models differs in many ways from the others, including magnetic geometry, computation methods, formulation of the heating rate, and treatment of multi-fluid effects. Our aim is simply to quantify the effects of time-dependent ionization on the observable line intensities in the region where the slow solar wind accelerates. Time-dependent ionization, as well as abundance variations, multi-fluid effects, non-Maxwellian electron distributions, heating rate assumptions, and the magnetic boundary condition at the solar surface, may all affect the predicted intensities on the level of a twofold factor. On the one hand, the NEI effects exceed the $\sim 30\%$ uncertainties expected from the atomic rates (Arnaud & Raymond 1992). Therefore, NEI is necessary to make the spectra predicted from the MHD models self-consistent for the parameters in the pseudostreamer.

4. Conclusions

Using the 3D global model for the WSM CR1913, we calculate the NEI state around a pseudostreamer. The predicted emissivities are obtained around this pseudostreamer, and the synthetic UVCS spatial intensity profiles for several lines, including Ly α , O VI 1032/1037 Å, Mg X 610 Å, Si XII 499/521 Å are compared with observations.

NEI is necessary to make accurate, self-consistent emissivity predictions from the MHD model for the parameters of the pseudostreamer. It significantly affects ion populations even at moderate coronal heights around the pseudostreamer. The

Mg X, Si XII, and Fe XII ion populations are higher in the NEI case at the upper heights, and the relative differences of ion population f_{diff} can be more than 0.9. In closed regions, the systematic siphon flows could reach tens of km s^{-1} and the ionization states therefore can differ from ionization equilibrium. However, f_{diff} is small because the plasma density is higher in closed regions than open regions, while in open regions it becomes large, especially in lower-density, higher-speed flows. On the other hand, the difference of ionic population between equilibrium ionization and NEI is insignificant for hydrogen and generally small for O VI. At the lowest height we consider, $1.41 R_{\odot}$, the differences between NEI and EI are small for all ions.

The synthetic Ly α , O VI doublet lines, and Mg 610 Å lines match UVCS observations well at low altitudes ($1.4 R_{\odot}$), but not at higher altitudes above around $2 R_{\odot}$. The reasons for the mismatch may include: variations in the elemental abundances due to gravitational settling or FIP variations; the assumption of a single temperature for protons, electrons, and metal ions; inaccuracy of the surface magnetic field used as a boundary condition for the MHD model. The differential flows and suprathermal electrons are also possible sources of discrepancy (Ko et al. 1998; Esser & Edgar 2001).

We note that Abbo et al. (2015) employed the H I and O VI line widths and the O VI doublet ratio to derive the ion temperatures, electron densities, and outflow speeds in a pseudostreamer. The line ratios and line widths measured by Abbo et al. are not directly affected by changes in the ionization state. However, changes in the ionization state among different streamlines along the LOS could affect the contributions to the total emission from those streamlines, and thereby indirectly affect the measured values.

We obtained the O^{7+}/O^{6+} ratio in central regions of this pseudostreamer. Zhao et al. (2013) used the in situ *Ulysses* O^{7+}/O^{6+} ratio as a measure of electron temperature at the freeze-in point, based on the assumption of local ionization equilibrium for the charge states. Their measurements show considerable scatter, as do the O^{7+}/O^{6+} ratios within the pseudostreamer in the model. The discrepancies between temperatures deduced from remote observations of the corona and from in situ observations at 1 au have been discussed in previous studies (e.g., Ko et al. 1997; Esser & Edgar 2000, 2001; Cranmer et al. 2007; Landi et al. 2014; Oran et al. 2015). On the other hand, our calculations show that the O^{7+}/O^{6+} ratio ranges from ~ 0.01 to ~ 0.08 in center regions of the pseudostreamer at the height $3.93 R_{\odot}$. The predicted O^{7+}/O^{6+} ratio in this model falls within the typical value of solar wind from in situ measurements, but is less than measurements reported in Zhao et al. (2013). However, the difference of O^{7+}/O^{6+} ratio between NEI and EI assumptions clearly varies, and can be as high as 4.5 times in this pseudostreamer, which indicates that NEI has a significant impact on deducing temperature based on in situ O^{7+}/O^{6+} ratio.

As mentioned in previous sections, a single fluid is assumed in this work. However, further study of the ionization calculation based on a multi-fluid model will be required because heavy ions in the corona are known to have different speeds (Buergi & Geiss 1986; Esser & Edgar 2001). In addition, better UV spectral data are needed, both to accurately measure the plasma parameters in the upper corona and to refine global models for more accurate traceback to connect

in situ measurements to specific coronal structures. Only then can we take NEI from a speculation to a diagnostic in its own right.

The authors thank Mark G. Linton for valuable comments and suggestions that helped to improve this paper. We also thank Lei Ni for improving the open source ionization calculation code: https://github.com/ionizationcalc/time_dependent_fortran/releases (Shen et al. 2015b). This research was supported by NASA grants NNX11AB61G and NNX12AB25G, and National Science Foundation SHINE grants AGS-1156076 and AGS-1358342 to the Smithsonian Astrophysical Observatory, and LWS under ROSES NNH13ZDA001N.

ORCID iDs

John C. Raymond  <https://orcid.org/0000-0002-7868-1622>
 Katharine K. Reeves  <https://orcid.org/0000-0002-6903-6832>
 Nicholas A. Murphy  <https://orcid.org/0000-0001-6628-8033>

References

- Abbo, L., Lionello, R., Riley, P., & Wang, Y.-M. 2015, *SoPh*, **290**, 2043
 Antiochos, S. K., Mikić, Z., Titov, V. S., Lionello, R., & Linker, J. A. 2011, *ApJ*, **731**, 112
 Arnaud, M., & Raymond, J. 1992, *ApJ*, **398**, 394
 Billings, D. E. 1966, *A Guide to the Solar Corona* (New York: Academic Press)
 Brueckner, G. E., Howard, R. A., Koomen, M. J., et al. 1995, *SoPh*, **162**, 357
 Buergi, A., & Geiss, J. 1986, *SoPh*, **103**, 347
 Colaninno, R. C., & Howard, R. A. 2015, *SoPh*, **290**, 997
 Cranmer, S. R. 2014, *ApJL*, **791**, L31
 Cranmer, S. R., Gardner, L. D., & Kohl, J. L. 2010, *SoPh*, **263**, 275
 Cranmer, S. R., van Ballegoijen, A. A., & Edgar, R. J. 2007, *ApJS*, **171**, 520
 Culhane, J. L., Harra, L. K., James, A. M., et al. 2007, *SoPh*, **243**, 19
 Dere, K. P. 2007, *A&A*, **466**, 771
 Dere, K. P., Landi, E., Young, P. R., et al. 2009, *A&A*, **498**, 915
 Esser, R., & Edgar, R. J. 2000, *ApJL*, **532**, L71
 Esser, R., & Edgar, R. J. 2001, *ApJ*, **563**, 1055
 Feldman, U., & Widing, K. G. 2003, *SSRv*, **107**, 665
 Frazin, R. A., Cranmer, S. R., & Kohl, J. L. 2003, *ApJ*, **597**, 1145
 Freeland, S. L., & Handy, B. N. 1998, *SoPh*, **182**, 497
 Gardès, B., Lamy, P., & Llebaria, A. 2013, *SoPh*, **283**, 667
 Gloeckler, G., Geiss, J., Balsiger, H., et al. 1992, *A&AS*, **92**, 267
 Hanneman, W. J., & Reeves, K. K. 2014, *ApJ*, **786**, 95
 Henke, T., Woch, J., Schwenn, R., et al. 2001, *JGRA*, **106**, 10597
 Hughes, J. P., & Helfand, D. J. 1985, *ApJ*, **291**, 544
 Hundhausen, A. J., Gilbert, H. E., & Bame, S. J. 1968, *JGR*, **73**, 5485
 Jin, M., Manchester, W. B., van der Holst, B., et al. 2012, *ApJ*, **745**, 6
 Ko, Y., Raymond, J. C., Li, J., et al. 2002, *ApJ*, **578**, 979
 Ko, Y.-K., Fisk, L. A., Geiss, J., Gloeckler, G., & Guhathakurta, M. 1997, *SoPh*, **171**, 345
 Ko, Y.-K., Geiss, J., & Gloeckler, G. 1998, *JGR*, **103**, 14539
 Kohl, J. L., Noci, G., Antonucci, E., et al. 1997, *SoPh*, **175**, 613
 Laming, J. M., Feldman, U., Drake, J. J., & Lemaire, P. 1999, *ApJ*, **518**, 926
 Laming, J. M., & Lepri, S. T. 2007, *ApJ*, **660**, 1642
 Landi, E., Del Zanna, G., Young, P. R., Dere, K. P., & Mason, H. E. 2012, *ApJ*, **744**, 99
 Landi, E., Oran, R., Lepri, S. T., et al. 2014, *ApJ*, **790**, 111
 Landi, E., Young, P. R., Dere, K. P., Del Zanna, G., & Mason, H. E. 2013, *ApJ*, **763**, 86
 Lepri, S. T., Zurbuchen, T. H., Fisk, L. A., et al. 2001, *JGRA*, **106**, 29231
 Linker, J., Lionello, R., Mikić, Z., Titov, V., & Antiochos, S. 2011, *ApJ*, **731**, 110
 Linker, J. A., Mikić, Z., Biesecker, D. A., et al. 1999, *JGR*, **104**, 9809
 Lionello, R., Linker, J. A., & Mikić, Z. 2009, *ApJ*, **690**, 902
 Masai, K. 1984, *Ap&SS*, **98**, 367
 Meng, X., van der Holst, B., Tóth, G., & Gombosi, T. I. 2015, *MNRAS*, **454**, 3697

- Mikić, Z., Linker, J. A., Schnack, D. D., et al. 1999, *PhPI*, **6**, 2217
- Mikić, Z., Lionello, R., Mok, Y., Linker, J. A., & Winebarger, A. R. 2013, *ApJ*, **773**, 94
- Murphy, N. A., Raymond, J. C., & Korreck, K. E. 2011, *ApJ*, **735**, 17
- Noci, G., Kohl, J. L., & Withbroe, G. L. 1987, *ApJ*, **315**, 706
- November, L. J., & Koutchmy, S. 1996, *ApJ*, **466**, 512
- Ofman, L., Abbo, L., & Giordano, S. 2013, *ApJ*, **762**, 18
- Oran, R., Landi, E., van der Holst, B., et al. 2015, *ApJ*, **806**, 55
- Oran, R., van der Holst, B., Landi, E., et al. 2013, *ApJ*, **778**, 176
- Rachmeler, L. A., Platten, S. J., Bethge, C., Seaton, D. B., & Yeates, A. R. 2014, *ApJL*, **787**, L3
- Raymond, J., Suleiman, R., van Ballegoijen, A., & Kohl, J. 1997, in *ESA Special Publication*, Vol. 415, *Correlated Phenomena at the Sun, in the Heliosphere and in Geospace*, ed. A. Wilson (Noordwijk: ESA), 383
- Raymond, J. C., McCauley, P. I., Cranmer, S. R., & Downs, C. 2014, *ApJ*, **788**, 152
- Reale, F. 2014, *LRSP*, **11**, 4
- Reeves, K. K., Freed, M. S., McKenzie, D. E., & Savage, S. L. 2017, *ApJ*, **836**, 55
- Reeves, K. K., Linker, J. a., Mikić, Z., et al. 2010, *ApJ*, **721**, 1547
- Riley, P., & Luhmann, J. G. 2012, *SoPh*, **277**, 355
- Schmelz, J. T., Reames, D. V., von Steiger, R., & Basu, S. 2012, *ApJ*, **755**, 33
- Schwadron, N. A., Fisk, L. A., & Zurbuchen, T. H. 1999, *ApJ*, **521**, 859
- Shen, C., Raymond, J., Murphy, N., & Lin, J. 2015a, *A&C*, **12**, 1
- Shen, C., Raymond, J. C., & Murphy, N. A. 2015b, *Non-Equilibrium Ionization Code*, doi:10.5281/zenodo.272609
- Shen, C., Reeves, K. K., Raymond, J. C., et al. 2013, *ApJ*, **773**, 110
- Sokolov, I. V., van der Holst, B., Oran, R., et al. 2013, *ApJ*, **764**, 23
- Stakhiv, M., Landi, E., Lepri, S. T., Oran, R., & Zurbuchen, T. H. 2015, *ApJ*, **801**, 100
- Strachan, L., Suleiman, R., Panasyuk, A. V., Biesecker, D. A., & Kohl, J. L. 2002, *ApJ*, **571**, 1008
- Usmanov, A. V., Goldstein, M. L., & Matthaeus, W. H. 2016, *ApJ*, **820**, 17
- van der Holst, B., Sokolov, I. V., Meng, X., et al. 2014, *ApJ*, **782**, 81
- von Steiger, R., Zurbuchen, T., Geiss, J., et al. 2001, *SSRv*, **97**, 123
- Wang, Y.-M., Grappin, R., Robbrecht, E., & Sheeley, N. R., Jr. 2012, *ApJ*, **749**, 182
- Wilhelm, K., Curdt, W., Marsch, E., et al. 1995, *SoPh*, **162**, 189
- Zhao, L., Gibson, S. E., & Fisk, L. A. 2013, *JGRA*, **118**, 2834
- Zurbuchen, T. H., Fisk, L. A., Gloeckler, G., & von Steiger, R. 2002, *GeoRL*, **29**, 66
- Withbroe, G. L., Kohl, J. L., Weiser, H., Noci, G., & Munro, R. H. 1982, *ApJ*, **254**, 361